Central Lancashire Online Knowledge (CLoK)

Title	Estimating masses of supermassive black holes in active galactic nuclei from the Hα emission line
Type	Article
URL	https://clok.uclan.ac.uk/53577/
DOI	https://doi.org/10.1051/0004-6361/202452746
Date	2025
Citation	Dalla Bontà, Elena, Peterson, B. M., Grier, C. J., Berton, M., Brandt, W. N., Ciroi, S., Corsini, E. M., Dalla Barba, B., Davies, R. et al (2025) Estimating masses of supermassive black holes in active galactic nuclei from the Hα emission line. Astronomy & Astrophysics, 696 (A48). ISSN 0004-6361
Creators	Dalla Bontà, Elena, Peterson, B. M., Grier, C. J., Berton, M., Brandt, W. N., Ciroi, S., Corsini, E. M., Dalla Barba, B., Davies, R., Dehghanian, M., Edelson, R., Foschini, L., Gasparri, D., Ho, L. C., Horne, K., Iodice, E., Morelli, L., Pizzella, A., Portaluri, E., Shen, Y., Schneider, D. P. and Vestergaard, M.

It is advisable to refer to the publisher's version if you intend to cite from the work.
https://doi.org/10.1051/0004-6361/202452746

For information about Research at UCLan please go to http://www.uclan.ac.uk/research/

Astronomy & Astrophysics

Estimating masses of supermassive black holes in active galactic nuclei from the Hα emission line

E. Dalla Bontà[1,2,3,⋆]🄳, B. M. Peterson[4,⋆⋆]🄳, C. J. Grier[5]🄳, M. Berton[6]🄳, W. N. Brandt[7,8,9]🄳, S. Ciroi[1,2],
E. M. Corsini[1,2]🄳, B. Dalla Barba[10,11]🄳, R. Davies[12]🄳, M. Dehghanian[13]🄳, R. Edelson[14]🄳, L. Foschini[11]🄳,
D. Gasparri[15]🄳, L. C. Ho[16,17]🄳, K. Horne[18]🄳, E. Iodice[19]🄳, L. Morelli[15]🄳, A. Pizzella[1,2], E. Portaluri[20]🄳,
Y. Shen[21,22]🄳, D. P. Schneider[7,8]🄳, and M. Vestergaard[23,24]🄳

[1] Dipartimento di Fisica e Astronomia "G. Galilei", Università di Padova, Vicolo dell'Osservatorio 3, I-35122 Padova, Italy
[2] INAF – Osservatorio Astronomico di Padova, Vicolo dell'Osservatorio 5, I-35122 Padova, Italy
[3] Jeremiah Horrocks Institute, University of Central Lancashire, Preston, PR1 2HE, UK
[4] c/o Tracy L. Turner, 205 South Prospect Street, Granville, OH 43023, USA
[5] Department of Astronomy, University of Wisconsin – Madison, Sterling Hall, 475 N. Charter St., Madison, WI 53706-1507, USA
[6] European Southern Observatory, Alonso de Córdova 3107, Casilla 19, Santiago 19001, Chile
[7] Department of Astronomy and Astrophysics, Eberly College of Science, The Pennsylvania State University,
525 Davey Laboratory, University Park, PA 16802, USA
[8] Institute for Gravitation and the Cosmos, The Pennsylvania State University, University Park, PA 16802, USA
[9] Department of Physics, The Pennsylvania State University, 525 Davey Laboratory, University Park, PA 16802, USA
[10] Università degli studi dell'Insubria, Via Valleggio 11, Como 22100, Italy
[11] Osservatorio Astronomico di Brera, Istituto Nazionale di Astrofisica (INAF), Via E. Bianchi 46, Merate 23807, Italy
[12] Max Planck Institute for Extraterrestrial Physics, Giessenbachstrasse, 85741 Garching bei München, Germany
[13] Department of Physics, Virginia Tech, Blacksburg, VA 24061, USA
[14] Eureka Scientific Inc., 2452 Delmer St. Suite 100, Oakland, CA 94602, USA
[15] Instituto de Astronomía y Ciencias Planetarias, Universidad de Atacama, Copayapu 485, Copiapó, Chile
[16] Kavli Institute for Astronomy and Astrophysics, Peking University, Beijing 100871, China
[17] Department of Astronomy, School of Physics, Peking University, Beijing 100871, China
[18] SUPA School of Physics and Astronomy, North Haugh, St. Andrews KY16 9SS, Scotland, UK
[19] INAF – Osservatorio Astronomico di Capodimonte, Via Moiariello 16, 80131 Napoli, Italy
[20] INAF – Osservatorio Astronomico d'Abruzzo, Via M. Maggini snc, I-64100 Teramo, Italy
[21] Department of Astronomy, University of Illinois Urbana-Champaign, Urbana, IL 61801, USA
[22] National Center for Supercomputing Applications, University of Illinois Urbana-Champaign, Urbana, IL 61801, USA
[23] DARK, Niels Bohr Institute, University of Copenhagen, Jagtvej 155, DK-2200 Copenhagen, Denmark
[24] Steward Observatory, University of Arizona, 933 N. Cherry Ave., Tucson, AZ 85721, USA

ABSTRACT

Aims. The goal of this project is to construct an estimator for the masses of supermassive black holes in active galactic nuclei (AGNs) based on the broad Hα emission line.
Methods. We made use of published reverberation mapping data. We remeasured all Hα time lags from the original data as we find that reverberation measurements are often improved by detrending the light curves.
Results. We produced mass estimators that require only the Hα luminosity and the width of the Hα emission line as characterized by either the full width at half maximum or the line dispersion.
Conclusions. It is possible, on the basis of a single spectrum covering the Hα emission line, to estimate the mass of the central supermassive black hole in AGNs with all three parameters believed to affect mass measurement – luminosity, line width, and Eddington ratio – taken into account. The typical formal accuracy in such estimates is of order 0.2–0.3 dex relative to the reverberation-based masses.

Key words. galaxies: active – galaxies: nuclei – quasars: emission lines – galaxies: Seyfert

1. Introduction

Astrophysical masses are measured by observing how they accelerate nearby objects. In the case of supermassive black holes at the centres of massive galaxies, masses are measured by modelling the dynamics of stars (e.g. van der Marel et al. 1998; Cretton et al. 1999; Gebhardt et al. 2003; Thomas et al. 2004; Valluri et al. 2004; Sharma et al. 2014), gas (e.g. Macchetto et al. 1997; Bower et al. 1998; Davies et al. 2004a,b; Davis et al. 2013; de Francesco et al. 2008; Hicks & Malkan 2008; Dalla Bontà et al. 2009) or megamasers (e.g. Wagner 2013; van den Bosch et al. 2016; Kuo et al. 2020) on spatially resolved scales. In the case of some relatively nearby active galactic nuclei (AGNs), the broad-line-emitting gas can be spatially resolved with interferometry (GRAVITY Collaboration 2018, 2020, 2021a,b, 2024). In other cases, the motions of gas on spatially unresolved scales can be modelled for mass measurement via the process of reverberation mapping

(RM; Pancoast et al. 2011; Grier et al. 2013b, 2017a; Pancoast et al. 2014). The ultraviolet, optical, and infrared spectra of AGNs are dominated by the presence of strong, Doppler-broadened emission lines whose flux varies in response to continuum variations that arise on accretion-disk scales. By mapping the response of the line-emitting gas as a function of line-of-sight velocity and time delay relative to the continuum variations, the kinematics of the line-emitting region and the mass of the central black hole can be determined. However, the technical demands of velocity-resolved (i.e. 'two-dimensional') RM are formidable compared to simpler measurement of the mean emission-line response time, or time lag, for an entire emission line (τ) and the emission-line width (ΔV; i.e. 'one-dimensional RM'; Blandford & McKee 1982; Peterson 1993, 2014) Compared to one-dimensional RM, two-dimensional RM requires more accurate relative flux calibration (including flat-fielding) as well as more accurate wavelength calibration and consistent spectral resolution. It has therefore been more common to measure the one-dimensional response of the emission line and the line width and combine them to determine the black-hole mass:

$$M_{\rm BH} = f \left(\frac{\Delta V^2\, c\tau}{G} \right) = f\mu, \qquad (1)$$

where the quantity in parentheses, known as the 'virial product' (μ), is in units of mass and is based on the two observables, line width and mean time delay. Under most circumstances (e.g. except when the continuum radiation or emission-line response is highly asymmetric), the mean time delay translates immediately into the mean radius of the line-emitting region, $R = c\tau$. Parameters that are not directly measured by this method, such as the inclination of the line-emitting region, are subsumed into the dimensionless factor f. In the absence of knowledge of these other parameters, it is common to use a mean value, $\langle f \rangle$, based on other statistical estimates of the masses, nearly always the relationship between the black-hole mass and the bulge stellar velocity dispersion, $M_{\rm BH}$–σ_*. This relationship was first recognized in quiescent galaxies (Ferrarese & Merritt 2000; Gebhardt et al. 2000a) but has also been identified in active galaxies (Gebhardt et al. 2000b; Ferrarese et al. 2001; Nelson et al. 2004; Watson et al. 2008; Grier et al. 2013a).

Even one-dimensional RM is resource-intensive, typically requiring a sequence of at least 30–50 high-quality spectroscopic observations over a suitable span of time (typically several times the light-crossing time, $\tau = R/c$) with an appropriate sampling rate (a sampling interval typically around $0.5R/c$ or less) and source variations that are conducive to successful reverberation detection. Fortunately, however, RM has shown that the emission-line region radii inferred from lags correlate with many different luminosity measures (L) approximately as $L \propto R^{1/2}$, thus enabling estimates of the central black-hole mass from a single spectroscopic observation. As the RM database has grown over time, it has become clear that this radius–luminosity (R–L) relation is oversimplified and that there is at least one more parameter that affects the radius of the line-emitting region, hereafter referred to as the broad-line region (BLR). The additional parameter is generally thought to be the Eddington ratio (i.e. the ratio of the true accretion rate to the Eddington accretion rate; e.g. Du et al. 2016, 2018; Du & Wang 2019; Grier et al. 2017b; Martínez-Aldama et al. 2019; Fonseca Alvarez et al. 2020). There is a long history of using the R–L scaling relation to estimate the BLR radius from a measured luminosity and combining this with the emission-line width to estimate the mass via Eq. (1), much of which we

reviewed in our earlier paper (Dalla Bontà et al. 2020, hereafter Paper I). Our investigation reported in Paper I supports the conclusion that the Eddington ratio is the missing parameter in the R–L relationship and demonstrates that this can be effectively be taken into account. In Paper I, we focused on updating the R–L relations for Hβ and C IV λ1549; the former because it has by far the best established RM database, and the latter because it affords a probe of the higher-redshift Universe and has been, we think unfairly, as we discuss in Paper I, deemed by some authors to be insufficiently reliable for mass estimates.

In the present work we focus on the other strong emission line in the optical, Hα λ6563. Compared to other strong broad emission lines in AGN spectra, Hα has been relatively neglected in RM studies. There are several reasons for this:

1. The sensitivity of the UV/optical detectors generally employed in ground-based RM studies limits the redshift range over which Hα can be observed. In the samples discussed in this paper, the highest-redshift AGNs are at $z \lesssim 0.15$.
2. The low space density of local highly luminous AGNs combined with cosmic downsizing means that the luminosity range that can be studied via Hα reverberation is limited compared to other broad emission lines. In the samples discussed here, there is only one AGN (3C 273 = PG 1226+023) with rest-frame 5100 Å luminosity at $L(5100\,\text{Å}) = \lambda L_\lambda(5100\,\text{Å}) > 10^{45}$ erg s^{-1} and a small handful with $L(5100\,\text{Å}) > 10^{44}$ erg s^{-1}.

Other deficiencies relative to Hβ (in some cases, but not all, Hβ and Hα are observed simultaneously) are as follows:

1. The amplitude of emission-line flux variability is generally higher in Hβ than in Hα (e.g. Peterson et al. 2004), which makes the variations easier to detect and characterize.
2. The continuum underneath Hα has more host-galaxy starlight contamination than that under Hβ, so the continuum variations are apparently stronger in the Hβ region of the spectrum and the starlight correction to the continuum luminosity at Hα is much larger and thus uncertainties are more impactful.
3. In many, but not all, cases, the highest fidelity relative flux calibration in the Hβ spectral region is achieved by assuming that the [O III] $\lambda\lambda$4959, 5007 fluxes are constant on reverberation timescales. These lines are more clearly separated from Hβ than potential narrow-line calibration sources around Hα (specifically [N II] $\lambda\lambda$6548, 6583 or [S II] $\lambda\lambda$6716, 6731). The [N II] lines in particular are much harder to separate from the Hα broad emission, which compromises them as internal flux calibrators and complicates measuring the broad Hα line width accurately. For two-dimensional reverberation studies (i.e. those that enable constructions of a velocity-delay map), the [N II] lines can be especially problematic.
4. At some modest redshifts, the Hα profile is badly contaminated by atmospheric absorption bands (i.e. the A band and B band), and accounting for this is not trivial.

However, recent developments in the study of nearby AGNs at high angular resolution in the near-infrared with both ground-based (e.g. GRAVITY at the VLTI) and space-based (JWST) telescopes has led to a renewed interest in reverberation results for Hα for direct comparison with mass determinations based on angularly resolved methods. For this reason, we decided to reconsider the issue of estimating AGN black-hole masses based on the Hα emission line. Our methodology largely follows that of Paper I. For consistency with Paper I, we assume $H_0 = 72$ km s^{-1} Mpc^{-1}, $\Omega_{\rm matter} = 0.3$, and $\Omega_\Lambda = 0.7$.

2. Observational database and methodology

2.1. Data

As in Paper I, we employed two high-quality databases for this investigation. First, we collected spectra, line-width measurements, and time series for reverberation-mapped AGNs that have appeared in the literature up through 2019. The objects included here are those from Paper I that also have Hα results available. Second, we included sources from the Sloan Digital Sky Survey Reverberation Mapping Project (hereafter SDSS-RM; Shen et al. 2015). While Paper I included only results from the first year of the project, here we examined the six-year database described by Shen et al. (2024), though as we explain below, only the first two years of spectroscopic monitoring plus a previous year of photometric monitoring are relevant to the present investigation.

Whenever possible, we used line-width measurements and flux or luminosity measurements from the published sources. In some cases where we had ready access to the data (notably the Palomar–Green quasars from Kaspi et al. 2000), we measured the line widths ourselves. In all cases, however, we remeasured the emission-line lags using the interpolated cross-correlation methodology (Gaskell & Peterson 1987) as implemented by Peterson et al. (1998) and modified by Peterson et al. (2004). We chose to remeasure all the SDSS-RM lags for two reasons.

Firstly, as described by Edelson et al. (2024), it is important to examine the effects of 'detrending' the light curves. Detrending means either fitting a low-order polynomial to the light curve and subtracting it from the data or convolving the light curve with a broad function, such as a Gaussian: either will remove the longest-term trends from the data. We did this because variations on timescales much longer than reverberation timescales can, because they contain so much power, lead to overestimates of the reverberation response timescale. Here we attempted a simple linear detrending, following Edelson et al. (2024), of the line and continuum light curves and used the time series that gives the 'best' results (generally defined by the smallest uncertainties in the lags). Typically we find that shorter light curves are unaffected by detrending, but in longer light curves the effects can be important.

Secondly, in the case of SDSS-RM data, we restricted our analysis to the first two years of spectroscopic observations ($56660 < \text{MJD} < 57195$) plus a preceding single year ($56358 < \text{MJD} < 56508$) of continuum measurements. Because the SDSS-RM quasars with Hα reverberation measurements are all fairly local and low luminosity, the sparse sampling of the continuum at earlier epochs and the continuum and lines at later epochs only adds noise to the cross-correlation results.

The data drawn from the literature are presented in Table A.1. Additional parameters associated with each source are drawn from Table A1 of Paper I[1]. As noted above, all lags were remeasured, but luminosities, adjusted to our adopted cosmology, and line widths are taken from the published sources. Some line-width measures were flagged by the original investigators as being particularly uncertain, usually because of various data quality issues. These values are denoted by preceding colons and are not used in any of the statistical analysis.

Table B.1 presents the parameter values for the SDSS-RM sample. Some additional necessary parameters appear in

---

[1] Associations between sources in Table A.1 of this paper and Table A1 of Paper I are obvious except in the case of Mrk 6. The three datasets used here were from MJDs 49250–49872, 49980–50777, and 53611–54803.

Table A2 of Paper I. Luminosities are based on parameters given by Shen et al. (2024), line widths are from Wang et al. (2019), and the Hα rest-frame lags are based on our own re-determinations. We give the range of epochs used in Col. 2 of Table B.1; we, however, eliminated epoch MJD 56713 from all the light curves as in many cases it was a clear outlier. The time span used for each individual source was the subset that gave the clearest results (i.e. those with the smallest errors and/or the least contamination by aliases).

2.2. Fitting methodology

In the remainder of this paper, we examine the relationships among various physical parameters via bivariate and multivariate fits, first, to establish fundamental relationships that will allow us to estimate central masses, and second, to employ these relationships to develop predictive relationships to estimate the central masses.

We employed a fitting algorithm described by Cappellari et al. (2013) that combines the least trimmed squares technique of Rousseeuw & van Driessen (2006) and a least-squares fitting algorithm that allows errors in all variables, as implemented in Paper I and by Dalla Bontà et al. (2018). Most fits are bivariate fits of the form

$$y = a + b(x - x_0), \tag{2}$$

where x_0 is the median value of the observable x. The fitting procedure minimizes the quantity

$$\chi^2 = \sum_{i=1}^{N} \frac{[a + b(x_i - x_0) - y_i]^2}{(b\Delta x_i)^2 + (\Delta y_i)^2 + \varepsilon_y^2}, \tag{3}$$

where Δx_i and Δy_i are the errors on the variables x_i and y_i, and ε_y is the standard deviation of the Gaussian describing the distribution of intrinsic scatter in the y parameter. The value of ε_y is adjusted iteratively so that the χ^2 per degree of freedom $\nu = N - 2$ has the value of unity expected for a good fit. The observed scatter is

$$\Delta = \left\{ \frac{1}{N - 2} \sum_{i=1}^{N} [y_i - a - b(x_i - x_0)]^2 \right\}^{1/2}. \tag{4}$$

The value of ε_y is added in quadrature to the formal error when y is used as a proxy for x.

As in Paper I, bivariate fits are intended to establish the physical relationships among the various parameters and to fit residuals, as described below. The initial mass estimation equations produced here are based on multivariate fits of the general form

$$z = a + b(x - x_0) + c(y - y_0), \tag{5}$$

where the parameters are as described above, plus an additional observed parameter y that has median value y_0. Similarly to linear fits, the plane fitting minimizes the quantity

$$\chi^2 = \sum_{i=1}^{N} \frac{[a + b(x_i - x_0) + c(y_i - y_0) - z_i]^2}{(b\Delta x_i)^2 + (c\Delta y_i)^2 + (\Delta z_i)^2 + \varepsilon_z^2}, \tag{6}$$

with Δx_i, Δy_i and Δz_i as the errors on the variables x_i, y_i, z_i, and ε_z as the sigma of the Gaussian describing the distribution of intrinsic scatter in the z coordinate; ε_z is iteratively adjusted so that the χ^2 per degrees of freedom $\nu = N - 3$ has the value of unity expected for a good fit. The observed scatter is

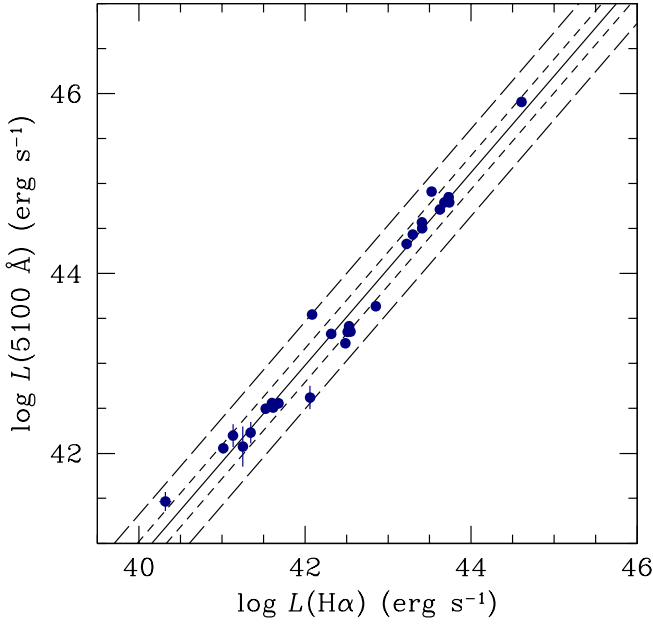$$\Delta = \left\{ \frac{1}{N - 3} \sum_{i=1}^{N} [z_i - a - b(x_i - x_0) - c(y_i - y_0)]^2 \right\}^{1/2}. \tag{7}$$

Fig. 1. Correlation between the luminosity of the broad Hα emission line and the starlight-corrected AGN continuum luminosity at 5100 Å. Only AGNs with host-galaxy starlight removal from the measured continuum based on HST high-resolution imaging are shown (Bentz et al. 2013), i.e. the AGNs listed in Table 1. The solid line represents the best fit to Eq. (2), with parameters given in line 1 of Table 1. The short-dash lines show the ±1σ envelope, and the long-dash lines show the ±2.6σ (99% confidence level) envelope.

3. Fits to the data

3.1. Fundamental relationships

One of the important results of Paper I is confirmation of the tight relationship between the luminosity of the broad Hβ emission line with that of the AGN continuum. This is important as it eliminates the necessity of quantifying the contribution of contaminating starlight to the observed continuum flux and also avoids possible complications from a contribution to the continuum from a jet[2]. This is even more critical in the Hα region of the spectrum where the starlight contamination is greater. Figure 1 shows the relationship between the Hα luminosity and the AGN luminosity at 5100 Å (taken from Paper I). The best-fit parameters for this relationship are given in line 1 of Table 1. The fit to this relationship shows that the luminosity of Hα can be used as a proxy for the AGN continuum at 5100 Å, which itself is tacitly used as a proxy for the AGN ionizing continuum, as is the case with Hβ.

Reverberation-based black-hole masses (Eq. (1)) are based on the measured lag τ of the emission-line flux variations relative to those of the continuum. Estimates of black-hole masses based on individual spectra – 'single epoch' (SE) masses – are enabled by the well-known correlation between BLR radius $R = c\tau$ and AGN luminosity (Kaspi et al. 2000, 2005; Bentz et al. 2006, 2009a, 2013, and additional historical references in Paper I). Figure 2 shows the relationship between the Hα lag and luminosity based on the data presented in Tables A.1 and B.1. The best-fit parameters to these data are given in line 2 of Table 1; the slope of the relationship is nearly exactly the canonical value

---

[2] We note, however, that only 3C 273 = PG 1226+023 and RMID 017 = SBS 1411+533 are flat-spectrum radio quasars; 3C 390.3 is also a radio source, but the jet is inclined to our line of sight.

$b = 0.5$. This fundamentally establishes justification for seeking a SE predictor based on the Hα line.

The other parameter needed to compute a reverberation-based mass is the emission-line width ΔV (Eq. (1)). Broad emission lines typically comprise multiple components, and the line width measured used in Eq. (1) should be based only on the emission-line components that are responding to the continuum variations. To isolate the variable part of the emission line, a root-mean-square residual spectrum (for brevity hereafter referred to as the 'RMS spectrum') is constructed. The mean spectrum is defined by

$$\overline{F}(\lambda) = \frac{1}{N} \sum_{1}^{N} F_i(\lambda), \qquad (8)$$

where $F_i(\lambda)$ is flux of the ith spectrum of the time series at wavelength λ and N is the total number of spectra. The RMS spectrum is then defined by

$$\sigma_{\mathrm{rms}}(\lambda) = \left\{ \frac{1}{N-1} \sum_{1}^{N} \left[F_i(\lambda) - \overline{F}(\lambda) \right]^2 \right\}^{1/2}. \qquad (9)$$

There are multiple parameters that might be used to characterize the emission-line width. Most commonly used are the full width at half maximum (FWHM) and the line dispersion, defined by

$$\sigma_{\mathrm{line}} = \left[\frac{\int (\lambda - \lambda_0)^2 P(\lambda)\, \mathrm{d}\lambda}{\int P(\lambda)\, \mathrm{d}\lambda} \right]^{1/2}, \qquad (10)$$

where $P(\lambda)$ is the line profile and λ_0 is the line centroid

$$\lambda_0 = \frac{\int \lambda P(\lambda)\, \mathrm{d}\lambda}{\int P(\lambda)\, \mathrm{d}\lambda}. \qquad (11)$$

Paper I presents detailed arguments that the line dispersion in the RMS spectrum σ_R is better than FWHM in the RMS spectrum, FWHM_R for computing reverberation masses. We also have carried out a preliminary investigation of other line-width measures and found that there are other good proxies for σ_R (Dalla Bontà & Peterson 2022), but this discussion is beyond the scope of the current work and will be pursued elsewhere. The aim here is then to determine, given a single spectrum, what line-width measure in the mean or a single spectrum (since the mean spectrum is a reasonable representation of a SE spectrum in the time series) is the better proxy for σ_R. Figure 3a shows the relationship between σ_R and the line dispersion in the mean spectrum, σ_M. Figure 3b shows the relationship between σ_R and FWHM in the mean spectrum, FWHM_M. Best-fit relationships between pairs of parameters are given in third and fourth lines of Table 1. As is the case with Hβ as described in Paper I, σ_M is an excellent proxy for σ_R. On the other hand, FWHM_M can also be used as a proxy for σ_R, but the relationship is not close to linear and the additional uncertainty introduced (ε_y) is more than twice as large as that introduced by σ_M.

At this point, we compared the virial products obtained with the Hα data in Tables A.1 and B.1 with the Hβ-based virial products we obtained in Paper I (see Fig. 4). For individual sources, in most cases the two virial products agree to within the uncertainties. A simple fit to this distribution, with resulting coefficients shown in line 5 of Table 1, confirms that the slope is less than unity and that the Hα-based virial product sightly exceeds the Hβ-based values with increasing mass. In the analysis that follows, we used the Hβ-based masses as our reference because the typical uncertainties (~0.113 dex) are considerably smaller than those associated with the Hα-based masses (~0.358 dex).

Table 1. Radius–luminosity, luminosity–luminosity, and line-width relations: $y = a + b(x - x_0)$.

Line (1)	x (2)	y (3)	$a \pm \Delta a$ (4)	$b \pm \Delta b$ (5)	x_0 (6)	ε_y (7)	Δ (8)	Figures (9)
1	$\log L(\mathrm{H}\alpha)$	$\log L_{\mathrm{AGN}}(5100\,\text{Å})$	43.530 ± 0.036	1.072 ± 0.036	42.513	0.174 ± 0.036	0.187	1
2	$\log L(\mathrm{H}\alpha)$	$\log \tau(\mathrm{H}\alpha)$	1.346 ± 0.036	0.497 ± 0.016	42.316	0.206 ± 0.036	0.242	2
3	$\log \sigma_{\mathrm{M}}(\mathrm{H}\alpha)$	$\log \sigma_{\mathrm{R}}(\mathrm{H}\alpha)$	3.185 ± 0.010	1.074 ± 0.053	3.227	0.058 ± 0.010	0.065	3a
4	$\log \mathrm{FWHM}_{\mathrm{M}}(\mathrm{H}\alpha)$	$\log \sigma_{\mathrm{R}}(\mathrm{H}\alpha)$	3.205 ± 0.025	0.699 ± 0.116	3.511	0.140 ± 0.023	0.140	3b
5	$\log \mu_{\mathrm{RM}}(\mathrm{H}\alpha)$	$\log \mu_{\mathrm{RM}}(\mathrm{H}\beta)$	7.049 ± 0.049	0.917 ± 0.078	6.956	0.081 ± 0.076	0.289	4

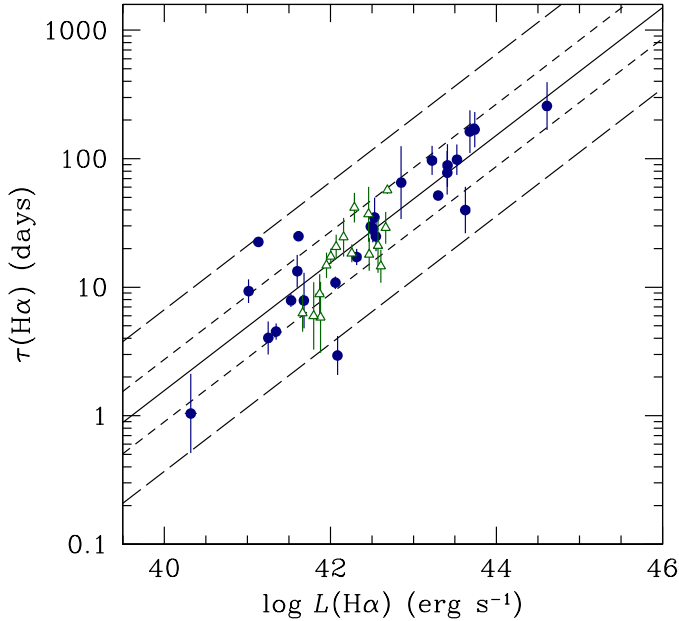**Fig. 2.** Time-delayed response of the broad Hα line as as a function of Hα luminosity. Since the response time is directly related to the BLR radius by $R = c\tau$, this is known as the R–L relationship. Blue circles are from the RM database (Table A.1) and green triangles are from SDSS-RM (Table B.1). The solid line shows the best fit to Eq. (2), with parameters given in the second line of Table 1. The short- and long-dashed line show the $\pm 1\sigma$ and $\pm 2.6\sigma$ envelopes, respectively.

3.2. Fits and corrections

The correlations identified above justify a search for a SE formula to estimate black-hole masses from Hα. As a first approximation, we began by trying to reproduce the Hβ RM virial product with the expectation that the BLR radius can be determined from the luminosity and that the line width in the mean spectrum can be used as a proxy for σ_{R}. The following equations were used:

$$\log \mu_{\mathrm{RM}}(\mathrm{H}\beta) = a + b\left[\log L(\mathrm{H}\alpha) - x_0\right] + c\left[\log \sigma_{\mathrm{M}}(\mathrm{H}\alpha) - y_0\right] \tag{12}$$

and

$$\log \mu_{\mathrm{RM}}(\mathrm{H}\beta) = a + b\left[\log L(\mathrm{H}\alpha) - x_0\right] + c\left[\log \mathrm{FWHM}_{\mathrm{M}}(\mathrm{H}\alpha) - y_0\right]. \tag{13}$$

The best fits to these equations are given in Table C.1. These can be used to produce initial SE predictors:

$$\log \mu_{\mathrm{SE}}(\mathrm{H}\alpha) = 6.996 + 0.501\left[\log L(\mathrm{H}\alpha) - 42.267\right] + 2.397\left[\log \sigma_{\mathrm{M}}(\mathrm{H}\alpha) - 3.227\right] \tag{14}$$

and

$$\log \mu_{\mathrm{SE}}(\mathrm{H}\alpha) = 7.082 + 0.583\left[\log L(\mathrm{H}\alpha) - 42.531\right] + 1.173\left[\log \mathrm{FWHM}_{\mathrm{M}}(\mathrm{H}\alpha) - 3.314\right]. \tag{15}$$

These data and their best fits are shown in Fig. 5, Eq. (14) in panel a and Eq. (15) in panel (b). In both cases, the slope b is shallower than unity, indicating that the line luminosity and line width are, by themselves, unable to accurately predict the reverberation measurement μ_{RM}. As noted above, in Paper I, we found that the residuals in this relationship were closely correlated with Eddington ratio, which is the ratio of actual mass-accretion rate relative to the maximum or Eddington rate. This finding is in agreement with the conclusions of others who have investigated the R–L relationship (e.g. Du et al. 2016, 2018; Grier et al. 2017b; Du & Wang 2019; Martínez-Aldama et al. 2019; Fonseca Alvarez et al. 2020). In the upper panels of Fig. 6, we show the residuals in the μ_{RM}–μ_{SE} relationship for Eqs. (14) (panel a) and (15) (panel b). As in Paper I, we computed a correction to the SE mass by fitting the relationship

$$\Delta \log \mu = \log \mu_{\mathrm{RM}} - \log \mu_{\mathrm{SE}} = a + b(\log \dot{m} - x_0). \tag{16}$$

Our assumptions and calculations of the Eddington ratio, the most important assumption being our use of the bolometric correction from Netzer (2019), are given in Paper I. The single modification here is that we used Eq. (2) with the relationship shown in Fig. 1 to substitute $L(\mathrm{H}\alpha)$ for $L_{\mathrm{AGN}}(5100\,\text{Å})$. The reason our correction works is because the simple assumptions we made to compute the Eddington ratio depend only on $L(\mathrm{H}\alpha)$ (or equivalently, $L_{\mathrm{AGN}}(5100\,\text{Å})$ or $L(\mathrm{H}\beta)$) and μ_{RM}, which are known for this sample. The best-fit parameters for Eq. (16) are given in lines 3 and 4 of Table 2. The bottom panels of Fig. 6 show the effect of this correction on the residuals.

Applying the correction of Eq. (16) to the SE masses in the top panels of Fig. 5 yields the corrected SE masses shown in the bottom panels of the same figure. The best-fit parameters for the revised relationship are given in lines 5 and 6 of Table 2 for the case of σ_{M} and $\mathrm{FWHM}_{\mathrm{M}}$-based masses, respectively. It should be noted that the slopes of these relationships are very close to the expected value of unity, indicating that the three variables identified – line luminosity, line width, and Eddington ratio – are sufficient to estimate the black-hole mass to fairly high accuracy.

4. Formulas for mass estimation

Our initial estimates (Eqs. (14) and (15)) can be combined with the Eddington rate correction (Eq. (16)), which we inverted to solve for an estimate of μ_{RM} based solely on $L(\mathrm{H}\alpha)$ and $\sigma_{\mathrm{M}}(\mathrm{H}\alpha)$.
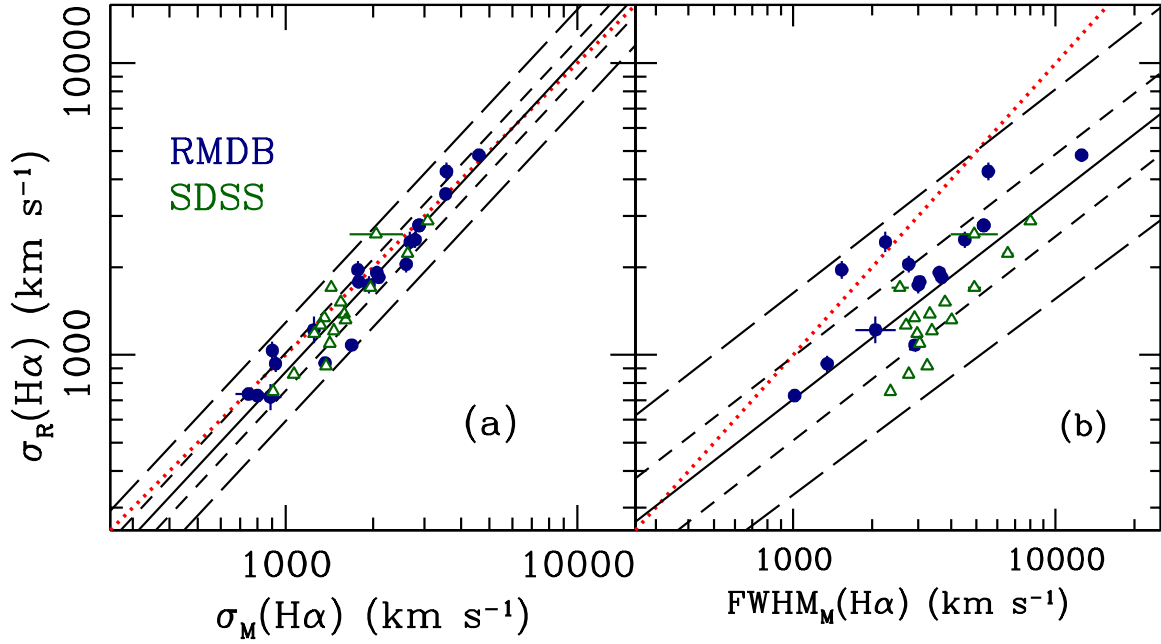
Fig. 3. Relationships between line-width measures. (a) Relationship between the Hα line dispersion in the RMS spectrum, $\sigma_R(H\alpha)$, and the mean spectrum, $\sigma_M(H\alpha)$. (b) Relationship between the Hα line dispersion in the RMS spectrum, $\sigma_R(H\alpha)$, and the FWHM in the mean spectrum, $\text{FWHM}_M(H\alpha)$. Blue points are from Table 1, (the reverberation mapping database or RMDB sample), green are from Table 2 (SDSS-RM sample). The solid lines are the best fit to Eq. (2) with coefficients from Table 1. The short- and long-dashed lines indicate the $\pm1\sigma$ and $\pm2.6\sigma$ envelopes. The dotted red lines indicate where the two measures are equal.
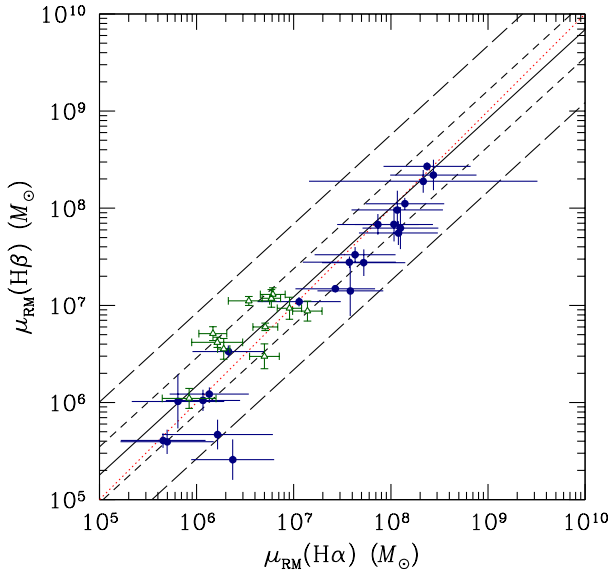

Fig. 4. Comparison between virial products based on the Hα data presented in Tables A.1 (blue circles) and B.1 (green triangles) and the virial products based on Hβ in Paper I. The dashed red line shows the locus where the two values are equal. The solid black line shows the best fit to the data. The short- and long-dashed lines show the $\pm1\sigma$ and $\pm2.6\sigma$ envelopes, respectively. The largest outlier is Mrk 202, which Bentz et al. (2010) flag as having an especially dubious Hα lag measurement.

This yields our equations for the corrected SE virial product estimator, with zero-points adjusted for convenience and for consistency with Paper I,

$$\log M_{SE} = \log f + 7.413 + 0.554 \left[\log L(H\alpha) - 42\right]$$
$$+ 2.61 \left[\log \sigma_M(H\alpha) - 3.5\right], \tag{17}$$

which has an associated uncertainty

$$\Delta \log M_{SE} = \left\{ (\Delta \log f)^2 + [0.554 \, \Delta \log L(H\alpha)]^2 \right.$$
$$\left. + [2.61 \, \Delta \log \sigma_M(H\alpha)]^2 \right\}^{1/2}. \tag{18}$$

We note that the intrinsic scatter, $\varepsilon_y = 0.219$, needs to be added in quadrature to the formal uncertainty.

Similarly, in the case where FWHM is used as the line-width measure,

$$\log M_{SE} = \log f + 6.688 + 0.812 \left[\log L(H\alpha) - 42\right]$$
$$+ 1.634 \left[\log \text{FWHM}_M(H\alpha) - 3.5\right], \tag{19}$$

which has an associated uncertainty of

$$\Delta \log M_{SE} = \left\{ (\Delta \log f)^2 + [0.812 \, \Delta \log L(H\alpha)]^2 \right.$$
$$\left. + [1.634 \, \Delta \log \text{FWHM}_M(H\alpha)]^2 \right\}^{1/2}. \tag{20}$$

Again, the intrinsic scatter, $\varepsilon_y = 0.332$, needs to be combined in quadrature with the formal uncertainty.

The mean scale factor is determined by calibrating the virial products μ_{RM} to the $M_{BH}-\sigma_*$ relations. Our adopted value, based on the most recent analysis of the largest database, is $\langle \log f \rangle = 0.683 \pm 0.150$ (Batiste et al. 2017). The error on the mean is $\Delta \log f = 0.030$ dex and this should also be folded into the mass estimate uncertainty.

5. Discussion

5.1. Limitations

The SE mass predictors developed here and in Paper I include sources in the luminosity range

$$41 \lesssim \log L_{AGN}(5100 \, \text{Å}) \, (\text{erg s}^{-1}) \lesssim 46$$
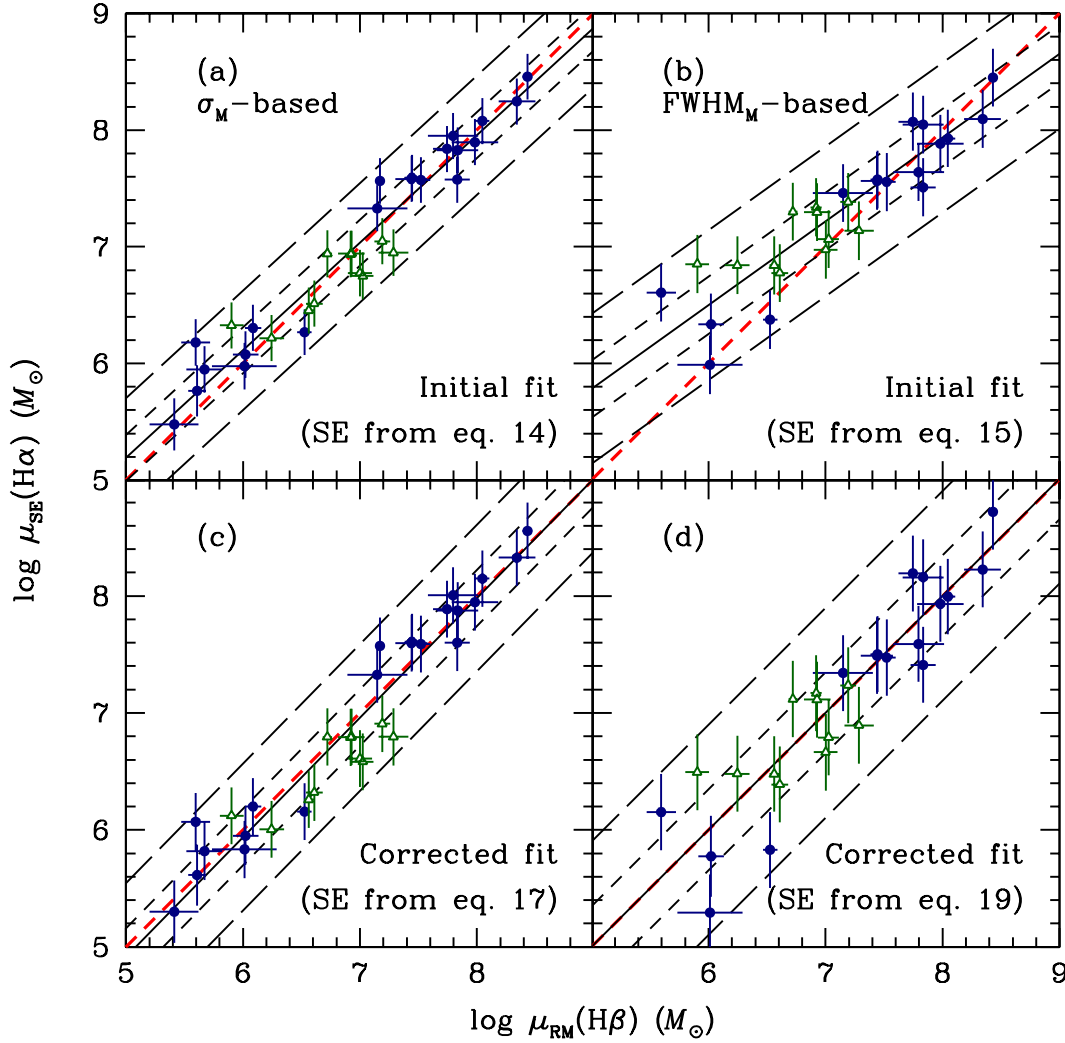
Fig. 5. Comparison between SE mass estimates and reverberation measurements. Upper: SE Hα-based virial product predictions using Eqs. (14) and (15) in panels (a) and (b), respectively. The coefficients for the best fit appear in the first two lines of Table 1. Blue circles are data from Table A.1, and green triangles are from Table B.1. The solid line is the best fit to the data, and the dotted red line shows where the measures are equal. The short- and long-dashed lines show the ±1σ and ±2.6σ envelopes, respectively. Lower: Corrected SE masses from Hα-based virial product predictions using Eq. (17) (panel c) and Eq. (19) (panel d), in both cases with log f = 0 arbitrarily.

Table 2. Initial, residual, and final fits: $y = a + b(x - x_0)$.

Line (1)	Basis (2)	x (3)	y (4)	$a + \Delta a$ (5)	$b + \Delta b$ (6)	x_0 (7)	ε_y (8)	Δ (9)	Figures (10)
Initial:									
1	σ_M	$\log \mu_{RM}$	$\log \mu_{SE}$	7.058 ± 0.036	0.922 ± 0.045	7.026	0.174 ± 0.035	0.196	5a
2	$FWHM_M$	$\log \mu_{RM}$	$\log \mu_{SE}$	7.323 ± 0.048	0.718 ± 0.064	7.149	0.231 ± 0.048	0.247	5b
Residual:									
3	σ_M	$\log \dot{m}$	$\Delta \log \mu$	-0.062 ± 0.033	-0.265 ± 0.072	-0.985	0.143 ± 0.030	0.168	6a
4	$FWHM_M$	$\log \dot{m}$	$\Delta \log \mu$	-0.175 ± 0.040	-0.602 ± 0.090	-1.134	0.162 ± 0.045	0.210	6b
Final:									
5	σ_M	$\log \mu_{RM}$	$\log \mu_{SE}$	6.988 ± 0.044	1.022 ± 0.055	7.026	0.219 ± 0.042	0.241	5c
6	$FWHM_M$	$\log \mu_{RM}$	$\log \mu_{SE}$	7.151 ± 0.067	1.000 ± 0.089	7.149	0.322 ± 0.067	0.345	5d

for the Balmer lines and

$$39.5 \lesssim L(1350\,\text{Å}) \, (\text{erg s}^{-1}) \lesssim 47$$

for C IV, though the sample size for the latter is very poor below log $L(1350\,\text{Å}) \approx 42$ (e.g. Fig. 9 of Paper I). This does, however, cover most of the known range of AGN activity. The range of

Eddington ratio covered by these estimators is

$$-2 \lesssim \log \dot{m} \lesssim 0$$

for the Balmer lines with extension to lower rates in C IV, as low as log $\dot{m} \approx -3$, but with poor sampling. This reaches close to the lowest Eddington ratios expected for broad-line AGNs.
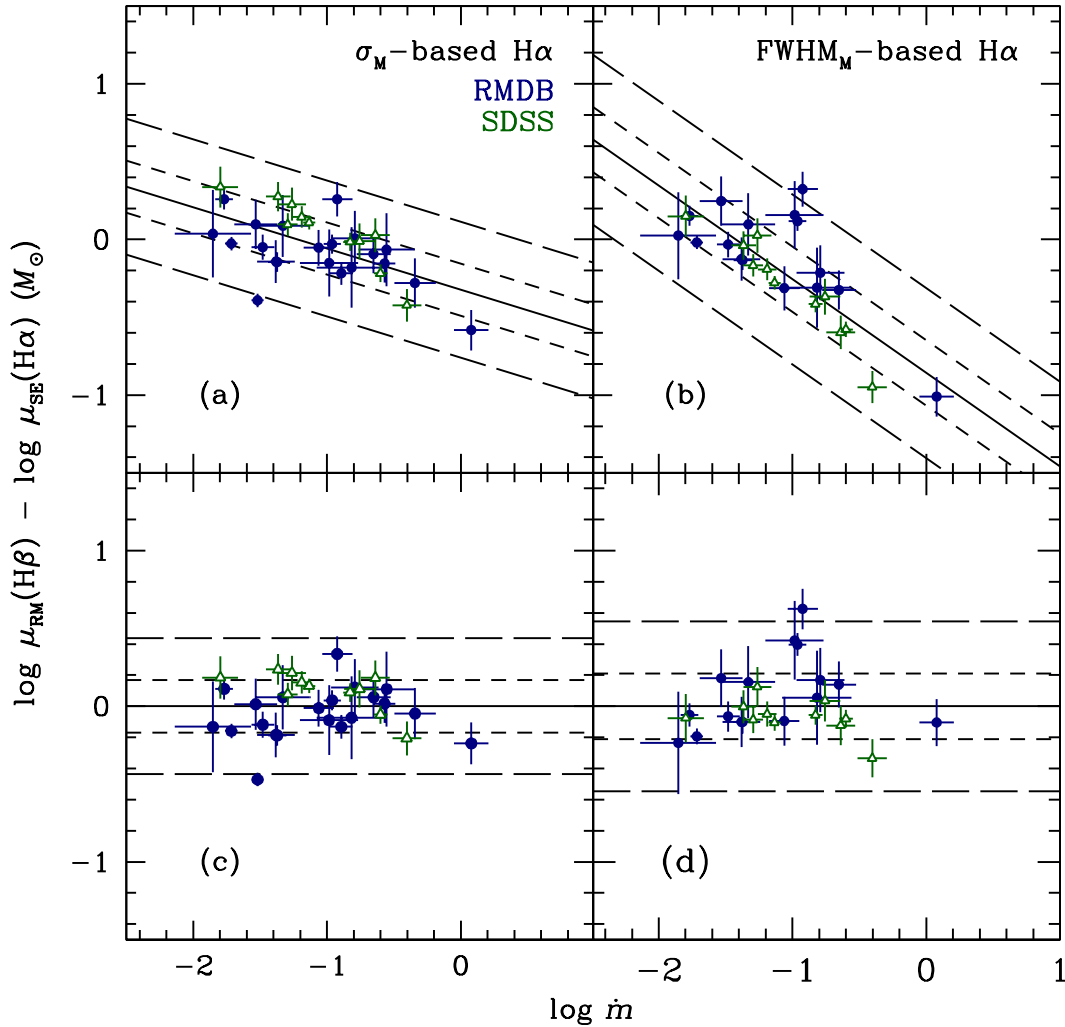
Fig. 6. Mass residuals as a function of Eddington rate. (a) Mass residuals (Eq. (16)), i.e. the difference between the measured reverberation virial products and those predicted by Eq. (12). The residuals are plotted vs the Eddington ratio. The solid line represents the best fit, the short-dashed lines the $\pm 1\sigma$ envelope, and the long-dashed line the $\pm 2.6\sigma$ envelope. Blue circles are from Table A.1, and green triangles are from Table B.1. (b) Mass residuals, i.e. the difference between the measured reverberation virial products and those predicted by Eq. (15). Panels (c) and (d) show residuals after subtraction of the best-fit relations shown in panels (a) and (b).

Extension to super-Eddington rates (i.e. $\dot{m} > 1$) remains to be explored.

5.2. On the importance of line-width measures

Much of this work has been focused on how the line-width measures are used. In particular, we have argued that if FWHM is used as ΔV in Eq. (1), the mass scale will be erroneously stretched. At larger line widths (higher mass at fixed luminosity), the ratio FWHM/σ is high so that the higher masses are overestimated by using FWHM. Similarly, for narrower lines (lower masses at fixed luminosity) FWHM/σ is low and thus lower masses are consequently underestimated by using FWHM. This point was made very clear by Rafiee & Hall (2011) who demonstrated this for fixed intervals of luminosity. The key point is that the mass scale is stretched at fixed luminosity.

This may obscure the fact that the single most important parameter in AGN black-hole mass estimation is luminosity. This is because the range of luminosity (over four orders of magnitude in the sample discussed here) is much larger than the range of line widths (spanning about a single order of magnitude in this sample). Figure 7 suggests that there is in fact a correlation between

luminosity and mass and a crude mass estimate can be made based on luminosity alone, which is tantamount to assuming that the range of Eddington ratio $\dot{m}$ is very narrow; indeed this realization led to a suggestion that the line width is superfluous and contains little if any additional leverage in estimating AGN black-hole masses (Croom 2011). This is true only if the line-width measurements are very inaccurate (as they sometimes are if they are measured from survey-quality data) or if one is willing to settle for a less than order-of-magnitude mass estimate. More importantly, however, one must be cognizant of the fact that selection effects militate against identification of sources in the upper left and lower right parts of this figure. Luminosity alone is simply not a very good predictor of black-hole mass.

5.3. Comparison with GRAVITY results

As noted earlier, there are a handful of sources that have been spatially resolved with the GRAVITY interferometer and have yielded mass measurements. Here we took luminosity and line-width measures from the published literature and used Eqs. (19) and (40) from Paper I to make comparisons between the GRAVITY measurements and our SE predictors. The results

Table 3. Comparison of SE estimates with GRAVITY measurements.

Source (1)	$\log(M/M_\odot)$ (GRAVITY) (2)	Ref. (3)	$\log(M/M_\odot)$ (SE) (4)	Line (5)	Ref. (6)
IRAS 09149−6206	$8.06^{+0.41}_{-0.57}$	1	8.331 ± 0.377	Hβ	5
Mrk 1239	7.47 ± 0.92	2	7.518 ± 0.377	Hβ	6
NGC 3783	$7.68^{+0.45}_{-0.43}$	3	7.551 ± 0.372	Hβ	7
3C 273	8.41 ± 0.18	4	9.403 ± 0.328	Hα	8
			9.383 ± 0.372	Hβ	8
			9.335 ± 0.372	Hβ	9
IC 4329A	$7.15^{+0.38}_{-0.26}$	2	7.563 ± 0.373	Hβ	10
			7.560 ± 0.372	Hβ	11,12
			8.484 ± 0.372	Hβ	6
PDS 456	$8.23^{+0.01}_{-0.49}$	2	9.784 ± 0.354	Hα	13
			9.358 ± 0.389	Hβ	13,14
			9.715 ± 0.373	Hβ	6
Mrk 509	$8.00^{+0.06}_{-0.23}$	2	8.419 ± 0.333	Hα	15
			8.510 ± 0.377	Hβ	15
			8.409 ± 0.373	Hβ	6

Notes. (1) GRAVITY Collaboration (2020); (2) GRAVITY Collaboration (2024); (3) GRAVITY Collaboration (2021a); (4) GRAVITY Collaboration (2018); (5) Pérez et al. (1989); (6) Li et al. (2024); (7) Bentz et al. (2021); (8) Kaspi et al. (2000); (9) Zhang et al. (2019); (10) Bentz et al. (2023); (11) Winge et al. (1996); (12) Collin et al. (2006); (13) Simpson et al. (1999); (14) Torres et al. (1997); (15) Osterbrock (1977).
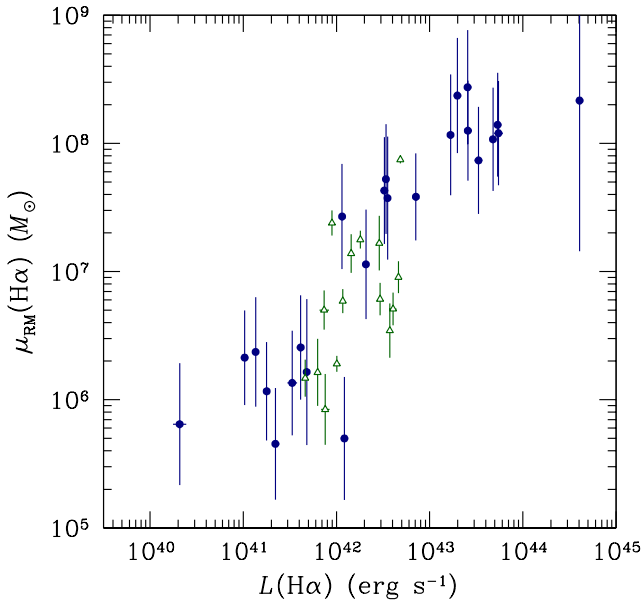

Fig. 7. Correlation between the virial product and luminosity of the Hα emission line. The apparent correlation between mass and luminosity is due to selection effects. Sources in the lower right (high luminosity, low mass) are generally excluded by the Eddington limit. Sources in the upper left (low luminosity, high mass) are scarce (a) because high mass objects are rare and therefore mostly at large distances, and thus faint, and (b) because their accretion rates are so low that they do not manifest themselves as AGNs.

Fig. 8. Comparison of the mass predictions from GRAVITY and SE estimates from the current work. Hβ-based SE masses are in black, Hα-based are in red. Note mass rather than the virial product is plotted.

are summarized in Table 3 and shown in Fig. 8. We assumed $\log f = 0.683$.

Figure 8 shows that the GRAVITY and SE-based masses are generally consistent at the low-mass end, but not at the high-mass end. In the case of IC 4329A, one SE-based prediction is considerably larger than the other two; this is because the estimate from Li et al. (2024) assumes ~2 mag of internal extinc-
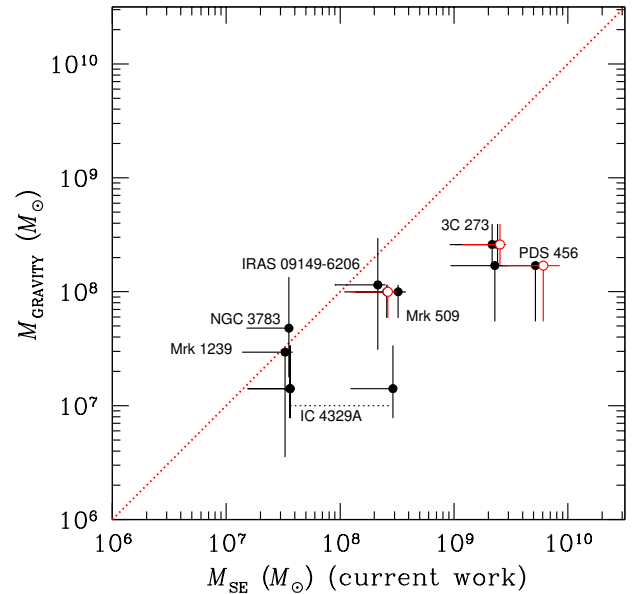
tion of the nucleus. The actual reverberation measurement, using measurements from Li et al. (2024), Eq. (A1) from Paper I, and $\log f = 0.683$) is ~7.75 in log solar units, closer to the other SE measurements than the estimate based on an internal extinction correction, which suggests that this correction is too large. For the two highest mass sources, 3C 273 and PDS 456, the GRAVITY and SE masses are in poorer agreement, and we note that in both cases, naïve application of the Eddington limits suggests both masses should exceed ~$10^9\,M_\odot$ (e.g. Nardini et al. 2015). In general, the SE estimates are in better agreement with the RM measurements than the GRAVITY measurements, when they are available.

Table 4. Fits to comparisons: $y = a + b(x - x_0)$.

Line (1)	x (2)	y (3)	$a \pm \Delta a$ (4)	$b \pm \Delta b$ (5)	x_0 (6)	ε_y (7)	Δ (8)	Figures (9)
1	$\log M_{\rm SE}$ (current)	$\log M_{\rm SE}$ (GH05)	7.685 ± 0.076	0.802 ± 0.011	7.854	$<10^{-3}$	0.152	9
2	$\log M_{\rm SE}$ (current)	$\log M_{\rm SE}$ (Cho23)	7.890 ± 0.064	0.852 ± 0.008	7.754	$<10^{-3}$	0.124	10
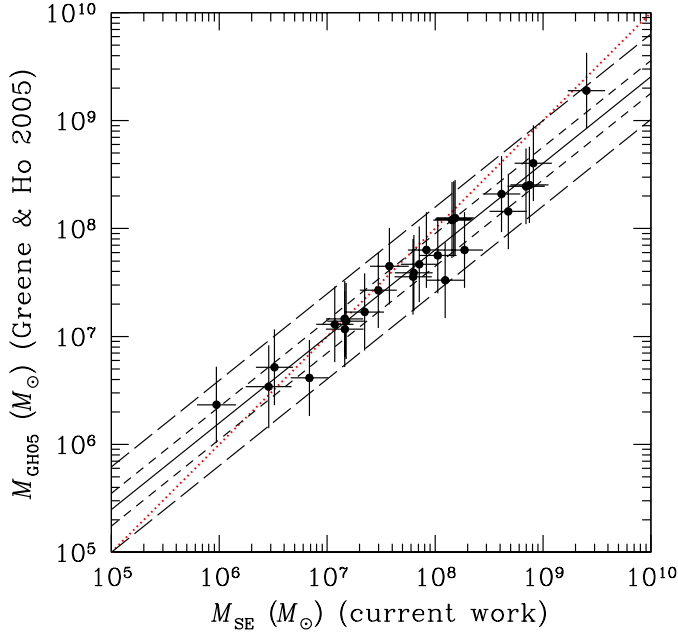
Fig. 9. Direct comparison of the mass predictions from Greene & Ho (2005) and from the current work. The dotted red line is the locus where the predictions are equal. The short-dash black lines show this $\pm1\sigma$ envelope and the long-dash lines show the $\pm2.6\sigma$ envelope. Note that mass rather than the virial product is plotted.
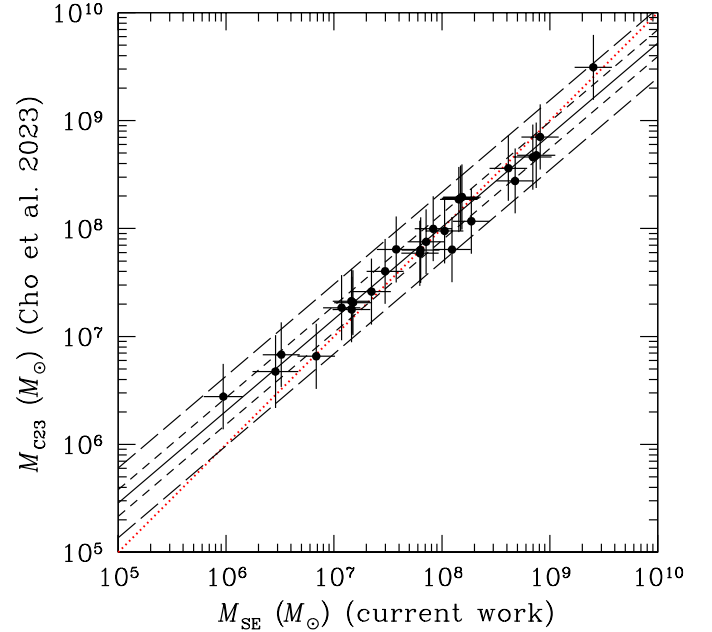
Fig. 10. Same as Fig. 10 but for the mass predictions from Cho et al. (2023).

5.4. Comparison with other single-epoch estimates

Here we compare our Hα-based mass predictions with those previously published. We considered first the early Hα-based mass predictor of Greene & Ho (2005); we rewrote their Eq. (6) as

$$\log M_{\rm GH05} = 7.331 + 0.55\,[\log L({\rm H}\alpha) - 42] + 2.06\,[\log {\rm FWHM}({\rm H}\alpha) - 3.5]. \quad (21)$$

Figure 9 shows a direct comparison of Eqs. (21) and (19) for the sample in Tables A.1 and B.1 (note that we plot the mass rather than the virial product). The best-fit results are given in line 1 of Table 4. Greene & Ho (2005) re-derived the relationship between the Hβ lag and the 5100 Å continuum, and essentially reproduced the result of Kaspi et al. (2005). This was prior to the first recognition that the contaminating starlight needs to be accounted for prior to deriving this relationship (Bentz et al. 2006); consequently the empirical relationship was steeper than the canonical value of 0.5. Empirical relationships among the 5100 Å continuum and the Hα and Hβ emission-line fluxes and between the Hα and Hβ line widths were also used. The scaling factor used was $f = 3/4$ (Netzer 1990), which was what was widely used prior the first empirical calibration (Onken et al. 2004).

We also compared our results with a more recent effort by Cho et al. (2023), whose database overlaps with ours consider-

ably. Their Eq. (6) can be written as

$$\log M_{\rm C23} = 7.505 + 0.61\,[\log L({\rm H}\alpha) - 42] + 2.0\,[\log {\rm FWHM}({\rm H}\alpha) - 3.5]. \quad (22)$$

The predictions from this equation are compared with those of our Eq. (19) in Fig. 10 (note that we plot the mass rather than virial product). The best-fit parameters are given in line 2 of Table 4. Again, the slope of the relationship between these two predictions is less than unity at least in part because of the lack of an Eddington ratio correction. Moreover, some of the underlying assumptions are so different:

1. Cho et al. (2023) assume a scaling factor value of $\log f = 0.05 \pm 0.12$ (Woo et al. 2015) when FWHM is used as the line-width measure. This corrects FWHM$_{\rm M}$ to $\sigma_{\rm M}$ for the mean ratio of $\langle{\rm FWHM}_{\rm M}/\sigma_{\rm M}\rangle$ (cf. Collin et al. 2006), but it does not account for the fact that the relationship between FWHM$_{\rm M}$ and $\sigma_{\rm M}$ is neither constant nor linear (e.g. Fig. 9 of Peterson 2014). Indeed, for the Hα lines examined in this investigation the width ratio cover the range

$$0.78 \lesssim {\rm FWHM}_{\rm M}/\sigma_{\rm M} \lesssim 2.73,$$

compared to the Gaussian value FWHM$/\sigma = 2.35$.
2. The slope we find for the Hα R–L relationship, $b = 0.497 \pm 0.016$, is shallower than their slope, $b = 0.61 \pm 0.04$.
3. Cho et al. (2023) assume that the mass scales as FWHM^2 while we find that the dependence of mass on FWHM is much shallower for Hα, as it is for Hβ (Paper I).

6. Conclusions

We have derived SE black-hole mass estimators based on the luminosity and line width of the broad Hα emission line (Eqs. (17) and (19)) with a typical formal uncertain of around 0.2–0.4 dex relative to the reverberation masses, depending on which emission-line and line-width measure are used. Both the Hα- and Hβ-based estimators were calibrated over the luminosity range $41 \lesssim \log L_{\mathrm{AGN}}(5100\,\text{Å}) \lesssim 46\,\mathrm{erg\,s^{-2}}$. Our treatment takes into account the three parameters known to affect black-hole mass: luminosity, line width, and Eddington ratio. As is the case with the Hβ emission line (Paper I), either the line dispersion (Eq. (10)) or the FWHM can be used as the line-width measure, though not interchangeably: the mass dependence on the line width is shallower for the FWHM than for the line dispersion.

References

Batiste, M., Bentz, M. C., Raimundo, S. I., Vestergaard, M., & Onken, C. A. 2017, ApJ, 838, L10
Bentz, M. C., Peterson, B. M., Pogge, R. W., Vestergaard, M., & Onken, C. A. 2006, ApJ, 644, 133
Bentz, M. C., Peterson, B. M., Netzer, H., Pogge, R. W., & Vestergaard, M. 2009a, ApJ, 697, 160
Bentz, M. C., Walsh, J. L., Barth, A. J., et al. 2009b, ApJ, 705, 199
Bentz, M. C., Walsh, J. L., Barth, A. J., et al. 2010, ApJ, 726, 993
Bentz, M. C., Denney, K. D., Grier, C. J., et al. 2013, ApJ, 767, 149
Bentz, M. C., Horenstein, D., Bazhaw, C., et al. 2014, ApJ, 796, 8
Bentz, M. C., Street, R., Onken, C. A., & Valluri, M. 2021, ApJ, 906, 50
Bentz, M. C., Onken, C. A., Street, R., & Valluri, M. 2023, ApJ, 944, 29
Blandford, R. D., & McKee, C. F. 1982, ApJ, 255, 419
Bower, G. A., Green, R. F., Danks, A., et al. 1998, ApJ, 492, L111
Cappellari, M., Scott, N., Alatalo, K., et al. 2013, MNRAS, 432, 1709
Carone, T. E., Peterson, B. M., Bechtold, J., et al. 1996, ApJ, 471, 737
Cho, H., Woo, J.-H., Wang, S., et al. 2023, ApJ, 953, 142
Clavel, J., Reichert, G. A., Alloin, D., et al. 1991, ApJ, 366, 64
Collin, S., Kawaguchi, T., Peterson, B. M., & Vestergaard, M. 2006, A&A, 456, 75
Cretton, N., de Zeeuw, P. T., van der Marel, R. P., et al. 1999, ApJS, 124, 383
Croom, S. M. 2011, ApJ, 736, 161
Dalla Bontà, E., & Peterson, B. M. 2022, Astronomische Nachrichten, 343
Dalla Bontà, E., Ferrarese, L., Corsini, E. M., et al. 2009, ApJ, 690, 537
Dalla Bontà, E., Davies, R. L., Houghton, R. C. W., et al. 2018, MNRAS, 474, 339
Dalla Bontà, E., Peterson, B. M., Bentz, M. C., et al. 2020, ApJ, 903, 112
Davies, R. I., Tacking, L. J., & Genzel, R. 2004a, ApJ, 602, 148
Davies, R. I., Tacconi, L. J., & Genzel, R. 2004b, ApJ, 613, 781
Davis, T. A., Bureau, M., Cappellari, M., et al. 2013, Nature, 494, 328
de Francesco, G., Capetti, A., & Marconi, A. 2008, A&A, 479, 355
Dietrich, M., Kollatschny, W., Peterson, B. M., et al. 1993, ApJ, 408, 416
Dietrich, M., Peterson, B. M., Grier, C. J., et al. 2012, ApJ, 757, 53
Doroshenko, V. T., Sergeev, S. G., Klimanov, S. A., Pronik, V. I., & Efimov, Y. S. 2012, MNRAS, 426, 416
Du, P., & Wang, J.-M. 2019, ApJ, 886, 42
Du, P., Lu, K.-X., Zhang, Z.-X., et al. 2016, ApJ, 825, 126
Du, P., Zhang, Z.-X., Wang, K., et al. 2018, ApJ, 856, 6
Edelson, R., Peterson, B. M., Gelbord, J., et al. 2024, ApJ, 973, 152
Ferrarese, L., & Merritt, D. 2000, ApJ, 539, L9
Ferrarese, L., Pogge, R. W., Peterson, B. M., et al. 2001, ApJ, 555, L79
Fonseca Alvarez, G., Trump, J. R., Homayouni, Y., et al. 2020, ApJ, 899, 73
Gaskell, C. M., & Peterson, B. M. 1987, ApJS, 65, 1
Gebhardt, K., Bender, R., Bower, G., et al. 2000a, ApJ, 539, L13
Gebhardt, K., Kormendy, J., Ho, L. C., et al. 2000b, ApJ, 543, L5
Gebhardt, K., Richstone, D., Tremaine, S., et al. 2003, ApJ, 583, 92
GRAVITY Collaboration (Sturm, E., et al.) 2018, Nature, 563, 657
GRAVITY Collaboration (Amorim, A., et al.) 2020, A&A, 643, A154
GRAVITY Collaboration (Amorim, A., et al.) 2021a, A&A, 648, A117
GRAVITY Collaboration (Amorim, A., et al.) 2021b, A&A, 654, A85
GRAVITY Collaboration (Amorim, A., et al.) 2024, A&A, 684, A167
Greene, J. E., & Ho, L. C. 2005, ApJ, 630, 122
Grier, C. J., Martini, P., Watson, L. C., et al. 2013a, ApJ, 773, 90
Grier, C. J., Peterson, B. M., Horne, K., et al. 2013b, ApJ, 764, 47
Grier, C. J., Pancoast, A., Barth, A. J., et al. 2017a, ApJ, 849, 146
Grier, C. J., Trump, J. R., Shen, Y., et al. 2017b, ApJ, 851, 21
Hicks, E. K. S., & Malkan, M. A. 2008, ApJS, 174, 31
Kaspi, S., Smith, P. S., Netzer, H., Maoz, D., Jannuzi, B. T., & Giveon, U. 2000, ApJ, 533, 631
Kaspi, S., Maoz, D., Netzer, H., Peterson, B. M., Vestergaard, M., & Jannuzi, B. T. 2005, ApJ, 629, 61
Kollatschny, W., Bischoff, K., Robinson, E. L., Welsh, W. F., & Hill, G. J. 2001, A&A, 379, 125
Kuo, C. Y., Braatz, J. A., Impellizzeri, C. M. V., et al. 2020, MNRAS, 498, 1609
Li, Y.-R., Hu, C., Yao, Z.-H., et al. 2024, ApJ, 974, 86
Macchetto, F., Marconi, A., Axon, D. J., et al. 1997, ApJ, 489, 579
Martínez-Aldama, M. L., Czerny, B., Kawka, D., et al. 2019, ApJ, 883, 170
Nardini, E., Reeves, J. N., Gofford, J., et al. 2015, Science, 347, 860
Nelson, C. H., Green, R. F., Bower, G., et al. 2004, ApJ, 615, 652
Netzer, H. 1990, Active Galactic Nuclei, 57
Netzer, H. 2019, MNRAS, 488, 5185
Onken, C. A., Ferrarese, L., Merritt, D., et al. 2004, ApJ, 615, 645
Osterbrock, D. E. 1977, ApJ, 215, 733
Pancoast, A., Brewer, B. J., & Treu, T. 2011, ApJ, 730, 139
Pancoast, A., Brewer, B. J., Treu, T., et al. 2014, MNRAS, 445, 3073
Pérez, E., Manchado, A., Pottasch, S. R., & García-Lario, P. 1989, A&A, 215, 262
Peterson, B. M. 1993, PASP, 105, 247
Peterson, B. M. 2014, Space Sci. Rev., 183, 253
Peterson, B. M., Wanders, I., Horne, K., et al. 1998, PASP, 110, 660
Peterson, B. M., Ferrarese, L., Gilbert, K. M., et al. 2004, ApJ, 613, 682
Rafiee, A., & Hall, P. B. 2011, MNRAS, 415, 2932
Reichert, G. A., Rodriguez-Pascual, P. M., Alloin, D., et al. 1994, ApJ, 425, 582
Rousseeuw, P., & van Driessen, K. 2006, Data Min. Knowl. Discovery, 12, 29
Sergeev, S. G., Pronik, V. I., Sergeeva, E. A., & Malkov, Y. F. 1999, ApJS, 121, 159
Sharma, S., Bland-Hawthorn, J., Binney, J., et al. 2014, ApJ, 793, 51
Shen, Y., Brandt, W. N., Dawson, K. S., et al. 2015, ApJS, 216, 4
Shen, Y., Grier, C. J., Horne, K., et al. 2024, ApJS, 272, 26
Simpson, C., Ward, M., O'Brien, P., et al. 1999, MNRAS, 303, L23
Stirpe, G. M., Winge, C., Altieri, B., et al. 1994, ApJ, 425, 609
Thomas, J., Saglia, R. P., Bender, R., et al. 2004, MNRAS, 353, 391
Torres, C. A. O., Quast, G. R., Coziol, R., et al. 1997, ApJ, 488, L19
Valluri, M., Merritt, D., & Emsellem, E. 2004, ApJ, 602, 66
van der Marel, R. P., Cretton, N., de Zeeuw, P. T., et al. 1998, ApJ, 493, 613
van den Bosch, R. C. E., Greene, J. E., Braatz, J. A., et al. 2016, ApJ, 819, 11
Wagner, J. 2013, A&A, 560, A12
Walsh, J. L., Minezaki, T., Bentz, M. C., et al. 2009, ApJS., 269, 39
Wanders, I., van Groningen, E., Alloin, D., et al. 1993, A&A, 269, 39
Wang, S., Shen, Y., Jiang, L., et al. 2019, ApJ, 882, 4
Watson, L. C., Martini, P, Dasyra, K. M., et al. 2008, ApJ, 682, L21
Winge, C., Peterson, B. M., Pastoriza, M. G., et al. 1996, ApJ, 469, 648
Woo, J.-H., Yoon, Y., Park, S., et al. 2015, ApJ, 801, 38
Zhang, Z.-X., Du, P., Smith, P. S., et al. 2019, ApJ, 876, 49

Appendix A: Data from the literature

Table A.1. Reverberation mapped AGNs (Hα).

Source (1)	References (2)	z (3)	$\tau(\mathrm{H}\alpha)$ (days) (4)	$\log L(\mathrm{H}\alpha)$ (erg s^{-1}) (5)	$\mathrm{FWHM_M}(\mathrm{H}\alpha)$ (km s^{-1}) (6)	$\sigma_\mathrm{M}(\mathrm{H}\alpha)$ (km s^{-1}) (7)	$\sigma_\mathrm{R}(\mathrm{H}\alpha)$ (km s^{-1}) (8)	$\log \mu_\mathrm{RM}(\mathrm{H}\beta)$ ($M_\odot$) (9)
PG 0026+129	1	0.14200	$98.16^{+28.28}_{-25.48}$	43.524 ± 0.041	1532 ± 32	1769 ± 17	1961 ± 135	7.833 ± 0.107
PG 0052+251	1	0.15445	$168.22^{+57.11}_{-48.74}$	43.738 ± 0.046	3605 ± 137	2054 ± 12	1913 ± 85	7.745 ± 0.122
Mrk 6	2,3	0.01881	$28.42^{+7.09}_{-6.51}$	42.513 ± 0.043	5322 ± 142	2870 ± 22	2780 ± 35	7.522 ± 0.078
Mrk 6	2,3	0.01881	$24.85^{+5.89}_{-7.06}$	42.548 ± 0.033	5322 ± 142	2870 ± 22	2780 ± 35	7.444 ± 0.060
Mrk 6	2,3	0.01881	$34.88^{+12.50}_{-12.11}$	42.531 ± 0.033	5322 ± 142	2870 ± 22	2780 ± 35	7.440 ± 0.137
PG 0804+761	1	0.10000	$170.93^{+14.26}_{-11.95}$	43.729 ± 0.026	2756 ± 16	2596 ± 9	2046 ± 138	8.047 ± 0.061
Mrk 110	4	0.03529	$29.61^{+3.76}_{-5.18}$	42.486 ± 0.043	...	...	...	6.770 ± 0.128
Mrk 142	5,6,7	0.04494	$2.94^{+0.94}_{-1.11}$	42.085 ± 0.034	1350 ± 39	925 ± 28	934 ± 61	5.596 ± 0.125
NGC 3516	8	0.00884	$13.35^{+2.87}_{-2.87}$	...	3238 ± 27	4152 ± 185	...	6.827 ± 0.164
SBS 1116+583A	5,6,7	0.02787	$4.02^{+1.38}_{-0.95}$	41.251 ± 0.030	2059 ± 359	1250 ± 39	1218 ± 125	6.022 ± 0.109
Arp 151	5,6,7	0.02109	$7.89^{+0.99}_{-0.86}$	41.525 ± 0.053	$:1852 \pm 7$	1367 ± 11	937 ± 34	6.087 ± 0.068
NGC 3783	9,10	0.00973	$13.32^{+3.56}_{-4.29}$	41.601 ± 0.044	...	...	...	6.787 ± 0.128
Mrk 1310	5,6,7	0.01956	$4.52^{+0.67}_{-0.65}$	41.345 ± 0.031	$:561 \pm 136$	887 ± 80	717 ± 75	5.609 ± 0.075
Mrk 202	5,6,7	0.02102	$22.49^{+1.80}_{-1.74}$	41.133 ± 0.034	$:463 \pm 38$	746 ± 77	734 ± 22	5.412 ± 0.209
NGC 4253	5,6,7	0.01293	$24.87^{+0.83}_{-0.73}$	41.616 ± 0.018	1013 ± 15	801 ± 42	726 ± 35	6.408 ± 0.054
PG 1226+023	1	0.15834	$256.83^{+40.88}_{-150.39}$	44.608 ± 0.035	3036 ± 49	2514 ± 47	$:2075 \pm 239$	8.277 ± 0.117
PG 1229+204	1	0.06301	$65.13^{+55.20}_{-23.75}$	42.852 ± 0.035	2996 ± 34	1931 ± 10	1737 ± 118	7.149 ± 0.257
NGC 4748	5,6,7	0.01463	$7.87^{+2.54}_{-4.64}$	41.681 ± 0.031	$:1967$	901 ± 34	1035 ± 74	5.670 ± 0.153
PG 1307+085	1	0.15500	$162.43^{+67.49}_{-56.50}$	43.679 ± 0.035	3685 ± 31	2090 ± 16	1843 ± 98	7.834 ± 0.176
NGC 5273	11	0.00362	$1.04^{+0.67}_{-0.80}$	40.318 ± 0.071	3032 ± 54	1781 ± 36	1783 ± 66	6.012 ± 0.278
PG 1411+442	1	0.08960	$108.46^{+62.92}_{-47.40}$	43.410 ± 0.015	2247 ± 44	2675 ± 13	2437 ± 196	7.796 ± 0.216
NGC 5548	12,13	0.01718	$17.17^{+2.54}_{-2.44}$	42.316 ± 0.028	...	...	1843 ± 98	7.038 ± 0.049
NGC 5548	5,6,7	0.01718	$10.85^{+1.31}_{-1.15}$	42.060 ± 0.028	$:1643 \pm 12$	3540 ± 40	3562 ± 141	7.172 ± 0.038
PG 1426+015	1	0.08657	$77.77^{+29.86}_{-30.11}$	43.407 ± 0.031	5534 ± 73	3563 ± 26	4254 ± 290	8.342 ± 0.157
PG 1613+658	1	0.12900	$39.80^{+18.16}_{-14.82}$	43.625 ± 0.026	6297 ± 85	4136 ± 65	...	7.705 ± 0.166
PG 1617+175	1	0.11244	$96.73^{+23.40}_{-26.91}$	43.224 ± 0.034	4503 ± 134	2780 ± 10	2483 ± 160	7.982 ± 0.198
3C 390.3	14	0.05610	$51.65^{+1.85}_{-1.96}$	43.297 ± 0.024	12563 ± 31	4607 ± 29	4839 ± 215	8.431 ± 0.041
NGC 6814	5,6,7	0.00521	$9.32^{+2.31}_{-1.50}$	41.015 ± 0.028	2909 ± 3	1686 ± 29	1082 ± 52	6.526 ± 0.061

Notes. Column (1) is the common name of the source. Column (2) provides references for the data (below). Column (3) is the redshift. Column (4) is the Hα time delay relative to the continuum, in the rest frame of the source. Column (5) is the luminosity of the Hα emission line. Columns (6), (7), and (8) are the Hα line width, characterized by FWHM in the mean spectrum, line dispersion in the mean spectrum, and line dispersion in the RMS spectrum, respectively, all in the rest frame of the source. Column (9) is the Hβ virial product from Paper I.

References. (1) Kaspi et al. (2000); (2) Sergeev et al. (1999); (3) Doroshenko et al. (2012); (4) Kollatschny et al. (2001); (5) Bentz et al. (2009b); (6) Bentz et al. (2010); (7) Walsh et al. (2009); (8) Wanders et al. (1993); (9) Reichert et al. (1994); (10) Stirpe et al. (1994); (11) Bentz et al. (2014); (12) Clavel et al. (1991); (13) Dietrich et al. (1993); (14) Dietrich et al. (2012).

Appendix B: Data from SDSS-RM

Table B.1. Reverberation mapped AGNs (SDSS Hα).

RMID (1)	z (2)	MJD Range (3)	τ(Hα) (days) (4)	$\log L$(Hα) (erg s^{-1}) (5)	FWHM$_{\rm M}$(Hα) (km s^{-1}) (6)	$\sigma_{\rm M}$(Hα) (km s^{-1}) (7)	$\sigma_{\rm R}$(Hα) (km s^{-1}) (8)	$\log \mu_{\rm RM}$(Hβ) ($M_\odot$) (9)
88	0.5175	56358–57195	$56.75^{+3.14}_{-4.35}$	42.686 ± 0.026	4899 ± 1017	2048 ± 431	2596 ± 11	$\cdots$
160	0.3598	56660–56838	$18.01^{+5.51}_{-5.94}$	42.467 ± 0.018	4014 ± 101	1609 ± 15	1318 ± 6	7.192 ± 0.068
191	0.4419	56660–56838	$17.39^{+2.37}_{-2.44}$	42.005 ± 0.034	2349 ± 61	907 ± 21	750 ± 15	6.245 ± 0.105
229	0.4698	56660–56838	$24.47^{+10.90}_{-5.10}$	42.159 ± 0.017	2555 ± 196	1437 ± 32	1702 ± 16	7.001 ± 0.103
252	0.2809	56660–56838	$14.81^{+3.61}_{-3.95}$	41.952 ± 0.014	8016 ± 184	3079 ± 56	2880 ± 8	$\cdots$
272	0.2629	56358–57195	$28.95^{+9.39}_{-7.05}$	42.665 ± 0.015	2692 ± 54	1321 ± 13	1265 ± 5	6.928 ± 0.114
320	0.2651	56660–56838	$20.58^{+5.13}_{-3.68}$	42.068 ± 0.021	3383 ± 49	1467 ± 36	1211 ± 6	7.026 ± 0.090
371	0.4726	56660–57195	$14.56^{+3.68}_{-4.80}$	42.607 ± 0.038	2901 ± 113	1358 ± 49	1341 ± 8	6.722 ± 0.039
377	0.3372	56660–56838	$5.98^{+3.00}_{-4.13}$	41.797 ± 0.027	2970 ± 67	1257 ± 20	1184 ± 10	6.562 ± 0.039
645	0.4739	56660–57195	$21.03^{+9.56}_{-10.90}$	42.573 ± 0.024	3245 ± 98	1377 ± 40	918 ± 4	6.921 ± 0.048
733	0.4547	56660–56838	$37.09^{+23.75}_{-9.95}$	42.459 ± 0.029	3797 ± 95	1548 ± 55	1517 ± 11	$\cdots$
768	0.2587	56660–56838	$18.34^{+3.09}_{-2.82}$	42.256 ± 0.026	6570 ± 321	2622 ± 63	2228 ± 4	$\cdots$
772	0.2491	56660–57195	$5.83^{+3.62}_{-3.78}$	41.880 ± 0.045	2763 ± 32	1069 ± 15	859 ± 2	5.903 ± 0.101
776	0.1164	56660–57195	$6.28^{+1.75}_{-2.37}$	41.665 ± 0.028	3038 ± 49	1418 ± 16	1097 ± 2	6.609 ± 0.071
840	0.2439	56660–56838	$8.84^{+3.95}_{-1.95}$	41.869 ± 0.052	4908 ± 283	1953 ± 39	1703 ± 4	7.287 ± 0.127

Notes. Column (1) is RMID: correspondence with SDSS identifier can be found in Table 1 of Grier et al. (2017b). Column (2) is redshift. Column (3) is range of dates (MJD) for which the time-series analysis was undertaken. Column (4) is the Hα lag relative to the continuum. Column (5) is the luminosity of the Hα line. Columns (6), (7), and (8) are the Hα line width, characterized by FWHM in the mean spectrum, line dispersion in the mean spectrum, and line dispersion in the RMS spectrum, respectively, all in the rest frame of the source. Column (9) is the reverberation virial product for Hβ from Paper I.

References. Line widths and luminosities are from Wang et al. (2019).

Appendix C: Multivariate relations

Table C.1. Multivariate relations: $z = a + b(x - x_0) + c(y - y_0)$.

Line	x	y	z	$a \pm \Delta a$	$b \pm \Delta b$	$c \pm \Delta c$	x_0	y_0	ε_z	Δ
1	$\log L$(Hα)	$\log \sigma_{\rm M}$(Hα)	$\log \mu_{\rm RM}$(Hβ)	6.996 ± 0.044	0.501 ± 0.064	2.397 ± 0.263	42.467	3.227	0.211 ± 0.042	0.230
2	$\log L$(Hα)	$\log$ FWHM$_{\rm M}$(Hα)	$\log \mu_{\rm RM}$(Hβ)	7.082 ± 0.066	0.583 ± 0.085	1.173 ± 0.247	42.531	3.314	0.310 ± 0.066	0.322